Evaluation of the structural integrity of solid rocket propellant by means of the viscoelastic fracture mechanics approach at low and medium strain rates

Mario Martínez [a], Raúl López [b], Jesús Rodríguez [a], Alicia Salazar [a,*]

[a] *Grupo de Durabilidad e Integridad Mecánica de Materiales Estructurales (DIMME), Escuela Superior de Ciencias Experimentales y Tecnología, Universidad Rey Juan Carlos, C/ Tulipán, s/n, 28933 Móstoles-Madrid, Spain*
[b] *Departamento de Optoelectrónica y Misilística, Campus "La Marañosa", Instituto Nacional de Técnica Aeroespacial (INTA), Ctra. M301 km 10.5, 28330 San Martín de la Vega-Madrid, Spain*

ABSTRACT

This work analyzes the influence of the displacement rate on the tensile properties and the fracture parameters, determined through a viscoelastic Fracture Mechanics approach, of carboxyl-terminated polybutadiene (CTPB) based solid composite propellants. Low and medium displacement rates attained in an electromechanical testing machine were inspected. From the true stress-true pseudo strain curves, the Young's modulus was not influenced by the displacement rate with value almost identical to the instantaneous modulus obtained from stress relaxation tests. The same trend was achieved for the Poisson's ratio, with a behavior close to incompressibility. On the other hand, the yield stress increased with the displacement rate rise. Regarding the fracture behavior, a strong dependency of the resistance curves in terms of both the viscoelasic J-integral and the viscoelastic crack tip opening displacement, CTOD, on the displacement rate was proved, being greater the fracture resistance as the displacement rate increases. Moreover, a linear relationship between the viscoelasic J-integral and the viscoelastic crack tip opening displacement was demonstrated. These results were confirmed by the fracture surfaces analysis. At low displacement rate, the damage nucleation and propagation occurred in the matrix while at high displacement rates, dewetting phenomena gave rise to rougher surfaces with damage initiation and growth mainly through the matrix – particle oxidizer interface.

1. Introduction

To guarantee satisfactory operation of solid propellant motors, structural integrity of the grains must be assessed. The structural integrity of solid propellants can be compromised by the presence of defects, being the cracks those which can produce the most catastrophic effects. During ignition pressurization, the extra exposed surface can cause an unexpected rise in gas pressure which can result in the motor bursting [1]. The source of defects may arise from the manufacturing process, thermal loads during storage and operation, vibrations during transportation and launch, etc. Apart from these extrinsic factors, the nonhomogeneous microstructure play an important role. Typical solid propellants are formed of different constituents with very distinct mechanical response. The matrix is usually a rubbery material, that behaves viscoelastically. The most representative reinforcements are the oxidizer, ceramic particles with an elastic mechanical response, and the fuel, normally powdered aluminum which presents an elastoplastic behavior owing to its metallic nature. This complex microstructure can give rise to large local stress concentrations even when there is a small overall strain, which can cause damage in form of dewetting along the particles/matrix interface with void nucleation, from which cracks can be initiated. This so different mechanical response of each constituent together with microstructural damage evolution leads to a clearly non-linear mechanical response [2]. Therefore, structural integrity can only be ascertained using a Non-Linear Fracture Mechanics (NLFM) approach. However, J-integral cannot be applied directly to viscous materials as the theory of Fracture Mechanics methodologies is intended for time-independent materials. Nevertheless, Knauss [3] and Schapery [4] developed the theoretical framework for viscoelastic fracture mechanics.

The fracture characterization of solid propellants is still an open question, partly due to the viscoelastic fracture mechanics needs of more evolutionary and experimental validation. There is scarce literature regarding the application of the viscoelastic J-integral, J_v, methodology for the fracture characterization of solid composite propellants. One of those few investigations is that of Bencher et al [5], who investigated the influence of the temperature and the strain rate on J_v, but they did not reach a definitive strain rate trend. To avoid the viscoelastic dissipation correction of the viscoelastic fracture mechanics, several strategies have been used for the fracture characterization of composite solid propellants within NLFM approach. Some researchers have used the wedge splitting test [6,7], or even the NLFM methodologies when the testing conditions are those in which the viscoelastic dissipation is negligible [8–10].

Despite there are some works on the fracture characterization of solid composite propellants, the lack of a non-uniform and standardized methodology for these viscoelastic materials with a strong non-linear mechanical response has led to very dissimilar results and with non well defined trends, in some cases. Therefore, the aim of this work is to determine the fracture parameters using the viscoelastic fracture mechanics approach of a carboxyl-terminated polybutadiene (CTPB) based propellant. The influence of the strain rate within the range achieved in an electromechanical testing machine on the J-integral and the crack tip opening displacement resistance curves will be analyzed as well as the micromechanisms of deformation and failure.

2. Theoretical background

2.1. The viscoelastic J integral

For the determination of the viscoelastic J-integral, J_v, firstly, the load (P) – load line displacement (u) record must be treated to remove the creep displacements occurring due to the viscoelastic behavior of the material. Schapery [4] considered that this viscoelastic behavior can be represented by an equivalent elastic model (linear or non-linear) through the use of pseudo variables, in which the stress state remains the same for both the viscoelastic material and the elastic counterpart and the pseudo displacement or displacement of the equivalent elastic problem, u^e, is obtained from the displacement of the viscoelastic material, u, through the hereditary integrals as follows:

$$u^e(t) = \frac{1}{E_R} \int_0^t E(t-\tau) \frac{\partial u(\tau)}{\partial \tau} d\tau \tag{1}$$

with E_R a reference modulus, usually chosen as the glassy or instantaneous modulus, and t the time variable. For a constant displacement or strain rate Eq. (1) can be rewritten as

$$u^e(t) = \frac{1}{E_R} \frac{u(t)}{t} \int_0^t E(t-\tau) d\tau \tag{2}$$

where $E(t)$ corresponds to the relaxation modulus. Thus, the $P-u$ record is converted into a $P-u^e$ diagram, in which the J_v can be computed for each point $P_i - u_i^e$ of the record as follows [19]:

$$J_{v,i} = J_{v,el,i} + J_{v,nl,i} \tag{3}$$

where $J_{v,el}$ and $J_{v,nl}$ are the elastic and non-linear components, respectively. $J_{v,nl}$ is equal to the plastic component of the J-integral in non-time-dependent materials such as metals [11]. Eq. (3) can be expressed as

$$J_{v,i} = \frac{K_{I,i}^2}{E^*} + \frac{\eta_{nl} U_{nl,i}}{B(W-a_0)} \tag{4}$$

where K_I is the mode I stress intensity factor, E^* is the elastic modulus either on plane stress ($E^* = E$) or plane strain ($E^* = E/(1-\nu^2)$, with ν the Poisson's ratio), W is the specimens width, B is the thickness, a_0 the

initial crack length, η_{nl} is a non-linear or plastic geometric factor and U_{nl} is the energy (area) under the load vs pseudo non-linear displacement, u_{nl}^e, curve given by:

$$U_{nl} = \int_0^{u_{nl}^e} P du_{nl}^e \tag{5}$$

with

$$u_{nl,i}^e = u_i - u_{el,i}^e = u_i^e - CP_i \tag{6}$$

where u_{el}^e is the pseudo elastic displacement calculated from the initial compliance of the sample, C, and the subindex i denotes the i-th value in the data set. The η_{nl} parameter can be determined by means of the load separation principle proposed by Ernst et al. [12,13]. This methodology is used in SENT configuration as this type of testing sample is not a standardized configuration and η_{nl} is clearly dependent on geometry and materials properties. This principle is based on the definition of the load, P, in terms of a geometric function, g, and a deformation function, H.

$$P = g\left(\frac{a}{W}\right) H\left(\frac{u_{nl}}{W}\right) \tag{7}$$

where the geometric function is a function of the crack length and the deformation function is a function of the non-linear displacement. Sharobeam and Landes [14] defined a separation parameter, $S_{i,j}$, which is the ratio of the loads of two samples with different stationary crack lengths, a_i and a_j, at a constant non-linear displacement:

$$S_{i,j} = \frac{P(a_i, u_{nl})}{P(a_j, u_{nl})}\bigg|_{u_{nl}} = \frac{g\left(\frac{a_i}{W}\right) H\left(\frac{u_{nl}}{W}\right)}{g\left(\frac{a_j}{W}\right) H\left(\frac{u_{nl}}{W}\right)}\bigg|_{u_{nl}} = \frac{g\left(\frac{a_i}{W}\right)}{g\left(\frac{a_j}{W}\right)} = constant \tag{8}$$

Eq. (8) entails that $S_{i,j}$ parameter is not dependent on the non-linear displacement and it is rather a constant for a given pair of stationary cracks. Therefore, the geometric function, g, can be constructed from $S_{i,j}$ as follows:

$$S_{i,j}\left(\frac{b_i}{W}\right) = Ag\left(\frac{b_i}{W}\right) \quad \text{for constant } b_j/W \tag{9}$$

where b is the remaining ligament ($b = W-a$) and A is a constant equal to $g(b_j/W)^{-1}$. Sharobean and Landes [15] demonstrated that the best fit of the experimental data was attained considering a power-law form for the geometric function:

$$S_{i,j}\left(\frac{b_i}{W}\right) = A\left(\frac{b_i}{W}\right)^{\eta_{nl}} \quad \text{for constant } b_j/W \tag{10}$$

3. Materials and experimental procedure

3.1. Materials

The material under study is a booster composite solid rocket propellant from a two-stage rocket motor with a matrix of carboxyl-terminated polybutadiene (CTPB) with 54 %wt of ammonium perchlorate (AP) oxidizer, 16 %wt micronized aluminum fuel and 3.6 %wt isodecyl pelargonate plasticizer. The size distribution of the AP particles is centered at 120 μm considering a normal distribution [16].

3.2. Relaxation tests

The relaxation function, $E(t)$, was determined through stress relaxation tests using parallelepipedic specimens with dimensions of 64 × 13 × 6.5 mm³. Three replica were tested in a DMA Q800 from TA Instruments with a 50 mm span accessory for three-point bending configuration. The selected temperature was 20 °C and the applied strain 1.5%, assuring linear-viscoelastic behavior [6,17], in 5 s and held for 30 min.

The relaxation modulus can be expressed by a Prony series:

$$E(t) = E_\infty + \sum_{i=1}^{N} E_i \exp(-t/\tau_i) \tag{11}$$

where E_i and τ_i are the coefficients of the Prony series of i-th order and E_∞ is the equilibrium modulus. A third order Prony series function was considered for fitting the experimental data using the least squares method according to the procedure described in [17]. The fitting was performed employing the Optimization Toolbox from MATLAB® and the only constraint applied was that the constants of the Prony series must remain positive.

3.3. Tensile tests

Tensile tests were carried out on dog-bone samples following the STANAG 4506 standard [18] in an electromechanical testing machine Instron 5967 with a load cell of ± 500 N. Tests were performed at room temperature and crosshead displacement rates of 5, 50 and 500 mm/min, corresponding with strain rates of 10^{-3} s^{-1}, 10^{-2} s^{-1} and 10^{-1} s^{-1}, respectively. Digital Image Correlation (DIC) technique was employed to obtain the strain field using a VIC-2D equipment. Three replica were tested for each condition.

3.4. Fracture tests

3.4.1. J-R curves

Single Edge Notched Tension (SENT) specimens with $70 \times 25 \times 12.5$ mm^3 in size were tested in the same Instron machine used for tensile tests at room temperature and at crosshead displacement rates of 0.5, 5, 50 and 500 mm/min. An initial sharp crack with 9.1 mm in length ($a/W = 0.364$) was introduced by sliding a sharp razor blade. A tool was manufactured to ensure crack front uniformity during the sharpening process and besides, all the specimens were inspected to guarantee no damage at the crack front. The tests were recorded to measure the crack growth at each instant time, using a VIC 2D equipment for tests at 0.5 and 5 mm/min and a Redlake MotionPro High Speed camera for higher displacement rates. Three replica were tested for each condition.

$J_v(\Delta a)$ or $J_v - R$ curves were obtained from the $P - u^e$ record after removing the displacement due to creep from the $P - u$ according to Eq. (2). For the determination of the $J_{v,i}$ at each point of the $P_i - u_i^e$ record the Eq. (4) was applied, with the stress intensity factor computed as:

$$K_I = \frac{P}{B\sqrt{W}} f\left(\frac{a}{W}\right) \tag{12}$$

where $f\left(\frac{a}{W}\right)$ is a dimensionless geometry factor, which for the SENT configuration is given by [19]:

$$f\left(\frac{a}{W}\right) = \frac{\sqrt{2\tan\left(\frac{\pi a}{2W}\right)}}{\cos\left(\frac{\pi a}{2W}\right)} \left[0.752 + 2.02\left(\frac{a}{W}\right) + 0.37\left(1 - \sin\left(\frac{\pi a}{2W}\right)\right)^3\right] \tag{13}$$

The crack length advancement at each instant, $\Delta a_i = a_i - a_0$, was determined optically and so, the J_v vs Δa curves were constructed. The presence of crack tip blunting zone was modelled attending to:

$$J_v = 2m\sigma_y\Delta a \tag{14}$$

with m a dimensionless constant that depends on stress state and on material properties and σ_y is the yield stress. On the other hand, the stable crack growth regime was described by a power law equation as:

$$J_v = C_1 \Delta a^{C_2} \tag{15}$$

where C_1 and C_2 are material constants with $C_2 \leq 1$. The energy at crack growth initiation or the critical value of J_v, $J_{v,c}$, was determined optically, occurring after the blunting regime is completed. Finally, to

guarantee plane strain state, the following condition must be fulfilled [20]:

$$B, (W - a_0), a_0 \geq 25 \frac{J_{v,c}}{\sigma_y} \tag{16}$$

Apart from fracture specimens with sharp cracks, blunt notch SENT specimens with notch length to width ratios of 0.364, 0.4, 0.5, 0.6 and 0.7 were tested to determine η_{nl}. The notch tip radius was of 1 mm.

3.4.2. CTOD-R curves

The measurement of the CTOD, δ, defined as the distance between two points at the crack tip resulting from the intersection of a 90° vertex with the crack flanks [19] was carried out by optical means. The CTOD is prone to undergoing extra displacements due to the viscoelastic behavior of the material, and the time-independent fracture parameter or pseudo CTOD, δ^e, was computed through the hereditary integrals as follows assuming constant δ rate

$$\delta^e(t) = \frac{1}{E_R} \frac{\delta(t)}{t} \int_0^t E(t - \tau) d\tau \tag{17}$$

Thus, the $\delta^e(\Delta a)$ or $\delta^e - R$ curves were determined. The critical value of δ^e, δ^e_c, corresponding to the initiation crack growth was also attained optically.

Finally, the fracture surfaces obtained from fracture tests were inspected via scanning electron microscopy (SEM) in a Hitachi S-3400 N microscope with the aim of determining the micromechanisms of deformation and failure.

4. Results and discussion

4.1. Relaxation function

Fig. 1 shows the relaxation function, $E(t)$, of the CTPB based solid composite propellant, with the solid line representing the mean value of Prony series parameters and the envelope of all the stress relaxation tests delimitated by dashed lines. The parameters of the third order Prony series are gathered in Table 1.

The reference modulus, E_R, or instantaneous modulus was taken equal to the modulus corresponding to $t = 0$, being $E(t = 0) = 9.7$ MPa.
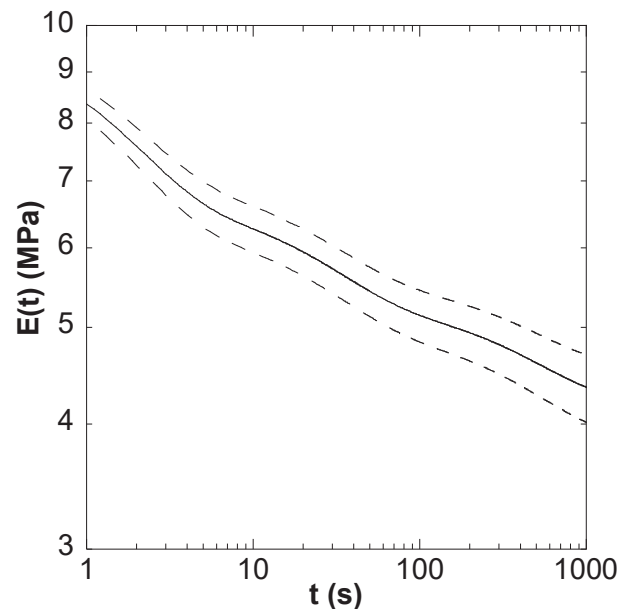

Fig. 1. Relaxation curve at room temperature of CTPB based solid propellant. Mean curve in solid line and the envelope of all the relaxation tests is delimitated by dashed lines.

Table 1
Prony series parameters of CTPB based propellant.

E_i (MPa)		τ_i (s)	
E_∞	4.2082	–	–
E_1	2.9665	τ_1	1.8197
E_2	1.3967	τ_2	28.5505
E_3	1.0835	τ_3	499.5837

Table 2
Tensile properties of CTPB based solid propellant such as the Young's modulus, E, the yield stress, σ_y, and the Poisson's ratio, ν, obtained from raw true stress-strain curves and true stress-pseudo strain diagrams (with superscript e).

$\dot{u}$ (mm/min)	E (MPa)	σ_y (MPa)	ν	E^e (MPa)	σ_y^e (MPa)
5	6 ± 1	0.49 ± 0.02	0.46 ± 0.02	10 ± 1	0.50 ± 0.02
50	10 ± 1	0.53 ± 0.01	0.46 ± 0.03	11 ± 1	0.54 ± 0.01
500	9.6 ± 0.3	0.61 ± 0.03	0.46 ± 0.02	10.3 ± 0.3	0.60 ± 0.03

4.2. Tensile properties

The representative true stress-strain curves of CTPB based solid composite propellant obtained at distinct displacement rates are displayed in Fig. 2. The continuous line corresponds to the stress (σ) – strain (ε) curves and the dotted lines represents the stress (σ) – pseudo strain (ε^e) curves. The pseudo-strain was calculated using the hereditary integrals as follows:

$$\varepsilon^e(t) = \frac{1}{E_R} \frac{\varepsilon(t)}{t} \int_0^t E(t-\tau)d\tau \tag{18}$$

As observed, the stress-strain curves exhibit two regions, the linear elastic region and the non-linear hardening region. This characteristic shape of the stress-strain curves is coincident with those attained by Wang et al. [21] in HTPB based solid composite propellants. The yield stress was determined from the intersection of the lines with slopes equal to those of the linear and non-linear hardening zones. Besides, increasing the displacement rate, the raw stress vs strain curves (solid lines) get closer to those pseudo curves (dashed lines), which are all comparable at low strains when damage is negligible. On the other hand, the separation among the stress- pseudo strain curves obtained at different displacement rate tends to occur beyond the yield stress, close to the failure region of the specimen.

The tensile properties of the CTPB based solid propellant such as the Young's modulus, the Poisson's ratio and the yield stress attained from both the raw stress-strain curves and the stress- pseudo strain diagrams (with superscript e) are summarized in Table 2. In case of the data obtained from raw stress-strain curves, the Young's modulus and the yield stress increase with increasing the displacement rate. On the other hand,

the Young's modulus attained from the stress-pseudo strain curves maintains constant with the displacement rate and agrees with the instantaneous modulus, E_R [22]. Instead, the yield stress values computed from the stress-pseudo strain curves are similar to those obtained from the raw stress-strain rate [21]. Finally, the Poisson's ratio was not influenced by the displacement rate and identical values were reported from both the raw and the pseudo stress-strain curves. Moreover, the values are very close to 0.5, indicating an almost incompressible behavior.

4.3. Fracture properties

4.3.1. Load separation property

The load vs pseudo non-linear displacement curves of notched samples of CTPB based solid propellant are shown in Fig. 3. The tests were run up to maximum displacements before crack growth from the notch occurred. In all cases, the load increases monotonically.

The separation parameter, $S_{i,j}$, versus pseudo non-linear displacement is displayed for the different notch length to width ratios taking the specimen with the smallest notch length, $a/W = 0.364$, as the reference curve in Fig. 4. All the plots show that S_{ij} maintains constant along the whole pseudo non-linear displacement range except for a limited zone at the beginning of the non-linear displacement range. This non-constancy $S_{i,j}$ region has been reported in both metals [14] and polymers [23,24] and it was associated to transition from elastic to plastic behavior. In this work, plastic behavior is replaced with non-linear behavior. Finally, in the range along which $S_{i,j}$ holds a constant value, the load is separable
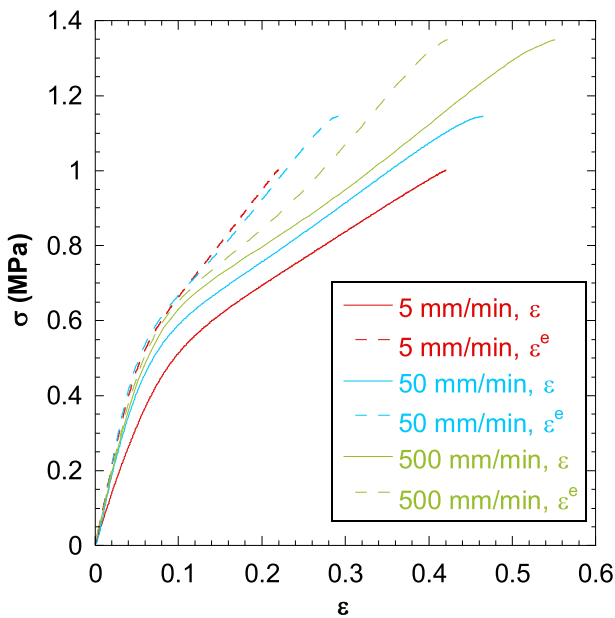
Fig. 2. Representative true stress vs true strain curves for crosshead displacement rates of 5, 50 and 500 mm/min. Raw curves in solid line, pseudo strain curves in dashed lines.
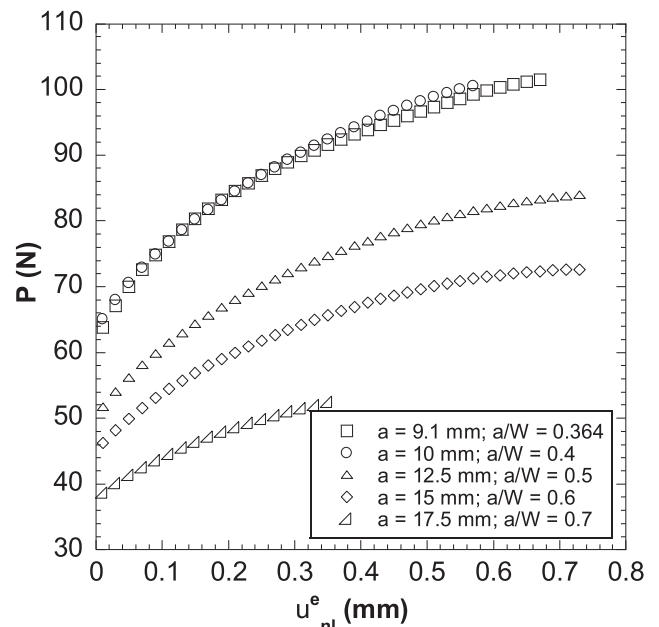
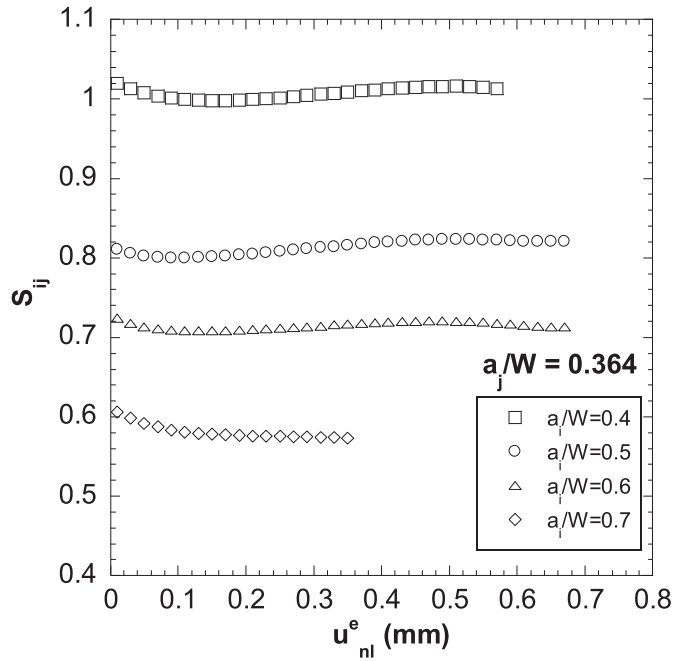**Fig. 3.** Load vs pseudo non-linear displacement curve of notched specimens.

Fig. 4. Separation parameter $S_{i,j}$ vs pseudo non-linear displacement for a reference $a_j/W = 0.36$.

Fig. 6. Representative load vs crosshead displacement curves at 0.5, 5, 50 and 500 mm/min. Raw curves in solid lines and their corresponding pseudo curves in dashed lines.

and can be written according to Eq. (7).

Once the load separation property has been verified, the geometry function g, and consequently, η_{pl} can be established. Fig. 5 plots the separation parameter $S_{i,j}$ values versus the remaining ligament, b_i/W and the fitting to Eq. (10) results in $A = 1.43$ and $\eta_{nl} = 0.76$. The value of η_{nl} agrees with that obtained by Han et al. [25].

4.3.2. J_v-R curves

Representative curves of load versus crosshead displacement at different displacement rates (solid lines) are shown in Fig. 6 together with their corresponding load versus pseudo crosshead displacement curves (dashed lines). Evident dependance on displacement rate is observed. The higher the rate, the higher the resistance of the sample.
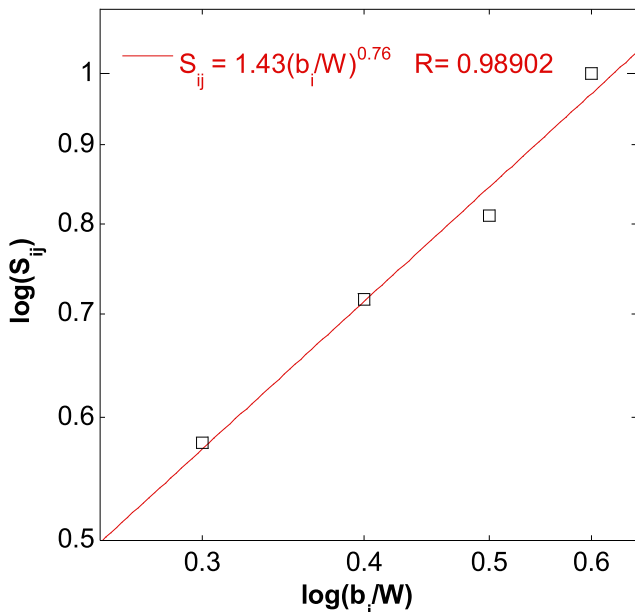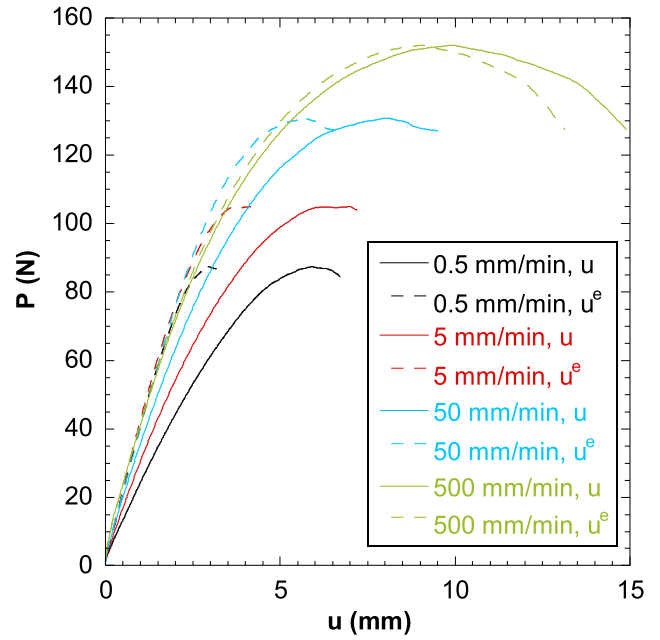
Also, the higher the rate, the less viscous dissipation correction is needed, and this is directly related to the fact that samples have less time to relax during the tests, since testing times are reduced significantly, up to one order of magnitude, when increasing the displacement rate. The load vs displacement curve obtained at a displacement rate of 500 mm/min and its analogous in terms of the pseudo displacement are extremely close to each other, with hardly viscous correction. Finally, another point worth mentioning is that at low displacements, the load vs pseudo displacement curves overlap, being this an indicative of a linear visco-elastic behavior until nonlinear behavior is produced by damage or crack growth initiation.

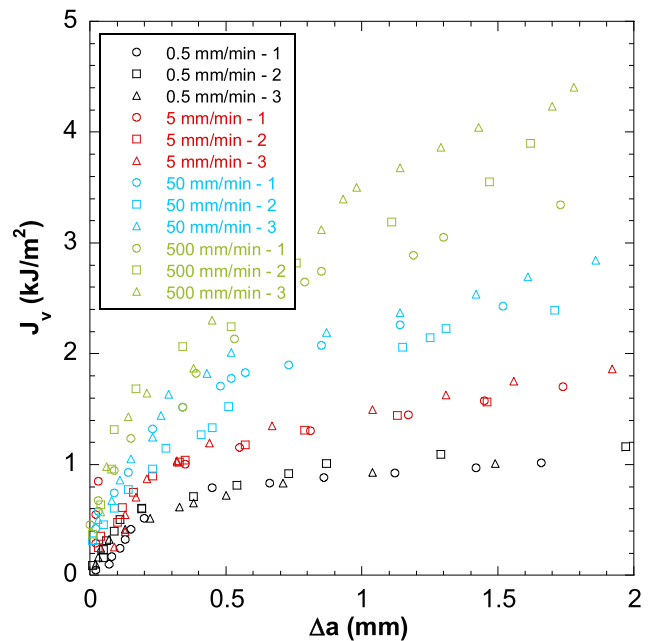$J_v - R$ resistance curves are presented in Fig. 7 and the values of the

Fig. 5. Separation parameter $S_{i,j}$ vs ligament on a double logarithmic scale.

Fig. 7. $J_v - R$ resistance curves at crosshead displacement rates of 0.5, 5, 50 and 500 mm/min.

parameters that describe these curves are collected in Table 3. The most striking is the strong dependence on the displacement rate, because the higher the displacement rate, the higher the energy needed for stable crack propagation and, consequently, the higher the energy needed for crack growth initiation, $J_{v,c}$ (Table 3), to the extent that the $J_{v,c}$ value at 500 mm/min is more than three times that of 0.5 mm/min. None of the critical values of J_v were in plane-strain conditions. Moreover, it seems that the steepness of the resistance curves is higher as the displacement rate increases. This is quantified by the exponent of the power law relationship (Eq. (15)) and Table 3 indicates that the main differences in C_2 occur between 50 and 500 mm/min, but they are not statically significant. Regarding the blunting zone, this extends to 0.2 or 0.3 mm of crack advancement depending on the displacement rate and the slope of the linear relationship of this regime is also gathered in Table 3. It is clear that this slope is also larger as the displacement rate increases. This trend is similar to that reported by Kim et al [7] in HTPB based solid propellants using wedge splitting tests.

4.3.3. CTOD-R curves

The $\delta^e - R$ resistance curves are shown in Fig. 8, and the values of the pseudo CTOD at crack growth initiation, δ^e_c, and the crack extension due to blunting at which crack growth starts, Δa_c, are gathered in Table 4. A similar trend to that exhibited by the $J_v - R$ resistance curves is observed. The higher the displacement rate, the higher the crack tip opening to produce the crack propagation and, consequently, the critical values of the pseudo CTOD for crack growth initiation. Regarding the blunting regime, the blunting extends farther before crack propagation starts as the displacement rate increases.

In order to determine the relationship between J_v and δ^e, Fig. 9 displays J_v vs δ^e. As observed, there seems to be a linear relationship, except for possibly the tests carried out at the lowest displacement rate where the load relaxation phenomena are more remarkable. In general, this evidences the viscoelastic behavior of the CTPB based solid propellants and the elastic behavior of the counterpart and so, this implies a small damage development in the process zone [19]. Therefore, the well-established relationship proposed by Wells [26] can be applied to this solid composite propellant for the fracture parameters in terms of the pseudo displacements:

$$J_v = m\sigma_y\delta^e \tag{19}$$

From the slope of the linear relationship, the dimensionless parameter, m, dependent on the stress state and the material properties can be inferred.

Table 5 shows the slope of the fitting of the experimental data to a linear law, $m\sigma_y$, the R^2 coefficient as well as the m dimensionless factor. The high value of R^2 supports the linear relationship between J_v and δ^e, and the value of m is close to 2, though this value disagrees with the one attained at the highest displacement rate of 500 mm/min. An attempt was made to explain this discrepancy by comparing the time to fracture initiation in fracture tests with the time to yielding in tensile tests. Both times were of the same order of magnitude despite the different constraint degree, and could not shed light. On the other hand, there are expressions in the literature where the relationship between J_v and δ^e (Eq. (19)) depends on the materials hardening exponent (for Ramberg-Osgood behavior in metals) [19]. Besides, viscoelastic behavior and/

Fig. 8. $\delta^e - R$ resistance curves at crosshead displacement rates of 0.5, 5, 50 and 500 mm/min.

Table 4
Fracture parameter from $\delta^e - R$ resistance curves.

$\dot{u}$ (mm/min)	Δa_c (mm)	δ^e_c (mm)
0.5	0.3 ± 0.1	0.6 ± 0.1
5	0.5 ± 0.3	0.8 ± 0.3
50	0.5 ± 0.1	1.2 ± 0.3
500	0.7 ± 0.3	2.4 ± 0.6

Fig. 9. $J_v - \delta^e$ relationship at crosshead displacement rates of 0.5, 5, 50 and 500 mm/min.

Table 3
$J_v - R$ resistance curves characteristic parameters.

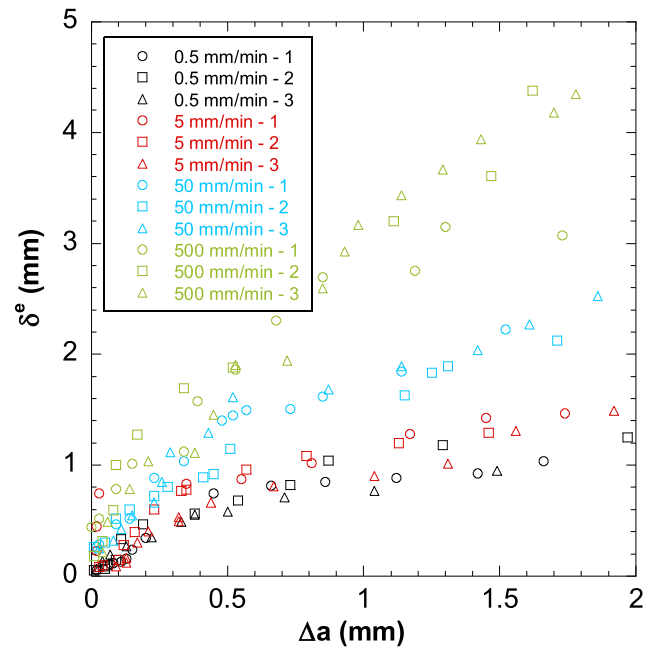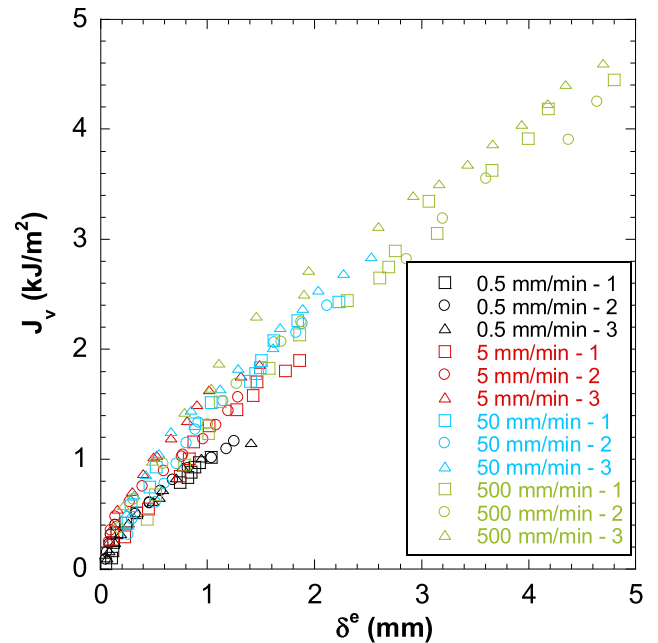| $\dot{u}$ (mm/min)	Blunting slope	Stable crack propagation		
	$2m\sigma_y$ (MPa)	$J_{v,c}$ (kJ/m^2)	C_1	C_2
0.5	3 ± 1	0.7 ± 0.1	0.9 ± 0.1	0.32 ± 0.03
5	5 ± 1	1.1 ± 0.2	1.4 ± 0.1	0.32 ± 0.02
50	4 ± 1	1.6 ± 0.3	2.1 ± 0.2	0.3 ± 0.1
500	6 ± 2	3 ± 1	3.1 ± 0.3	0.4 ± 0.1

Table 5
Fracture parameters describing the $J_v - \delta^e$ relationship.

$\dot{u}$ (mm/min)	$m\sigma_y$(kJ/m^2)	R^2	m
0.5	0.85 ± 0.06	0.977 ± 0.009	2.0 ± 0.2*
5	1.03 ± 0.09	0.985 ± 0.008	2.1 ± 0.2
50	1.05 ± 0.06	0.990 ± 0.001	1.9 ± 0.1
500	0.86 ± 0.04	0.993 ± 0.002	1.43 ± 0.07

* An extrapolated value of the yield stress at 0.5 mm/min has been used.

or fracture mechanism may influence this relationship. As seen in Fig. 2, displacement rate affects the hardening region and viscoelasticity, leading to changes in fracture mechanisms (explaination given later, see Fig. 10); therefore, we are aware that further research must be carried out to help widening the knowledge about the relationship between J_v and δ^e, especially in viscoelastic materials.

4.3.4. Micromechanisms of deformation and failure
SEM images from the fractographical analysis are shown in Fig. 10. Firstly, the roughness of the fracture surfaces increases with the displacement rate and no trace of oxidizer particles is observed (Fig. 10a and Fig. 10b). This clearly indicates that the damage initiation occurs in the elastomeric matrix and subsequently continues its propagation through it. This could be accounted for the strong matrix relaxation phenomena occurring at low displacement rates, which entails a decrease in the matrix strength in comparison to the matrix – oxidizer particles strength. Secondly, at higher displacement rates (Fig. 10c and Fig. 10d), a more energetic process is involved, which results not only in larger roughness along the fracture surface and more tearing in the matrix, but also damage located at the matrix-particle interface in form of holes or cracks. This process is known as dewetting and can be observed in Fig. 10d, taken at the fracture surface of a test at 500 mm/min. The oxidizer particles are clean with no trace of matrix in their surface. Finally, the increase in the surface roughness and the change of the damage nucleation and propagation from the matrix to the matrix

and matrix-oxidizer particle interface with the increase in the displacement rate seems to be behind of the better fracture resistance at higher displacement rates.

5. Conclusions

This work analyzes the influence of the displacement rate on the tensile and fracture properties of a CTPB based solid composite propellant. The displacement rates evaluated were in the low and medium range, attained with an electromechanical testing machine. For the fracture characterization, the viscoelastic fracture mechanics approach was applied and both the resistance curves in terms of the viscoelastic J-integral and crack tip opening displacement were determined.

The tensile properties were strongly influenced by the displacement rate. The parameters obtained from the true stress – true strain curves revealed that both the Young's modulus and the yield stress increase with the displacement rate. On the other hand, the parameters determined from the true stress – true pseudo strain curves showed that the Young's modulus was unaffected by the displacement rate with a value identical to the instantaneous modulus inferred from the stress relaxation analysis, while the yield stress values were similar to those obtained from the raw curves, following the same trend with the displacement rate. Finally, the Poisson's ratio was not influenced by the displacement rate and presented values close to 0.5.

Regarding the fracture characterization, it has been demonstrated that the load separation principle is valid for the CTPB based solid composite propellant. Both the viscoelastic J-integral and CTOD curves were strongly dependent on the displacement rate, with improved fracture resistance as the displacement rate increases. Besides, a linear relationship has been proved between the viscoelastic J-integral and the viscoelastic CTOD, leading to a dimensionless parameter, m, close to 2. Finally, these results were corroborated by the fractographic analysis. At low displacement rates, the damage initiated and propagated in the matrix resulting in less rougher surfaces than those of the specimens tested at high displacement rates. In these, the damage tended to
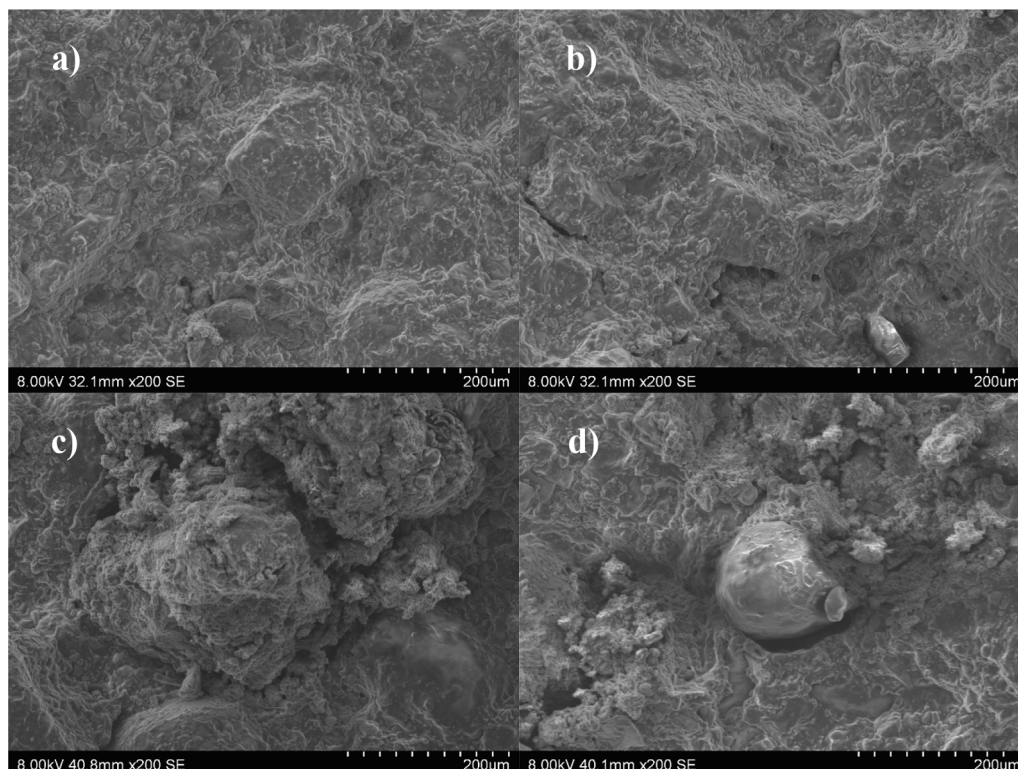

Fig. 10. Fracture surfaces obtained from fracture tests at displacement rates of a) 0.5 mm/min, b) 5 mm/min, c) 50 mm/min and 500 mm/min.

nucleate and to propagate along the matrix – oxidizer particles interface, giving rise to the known dewetting phenomenon.

CRediT authorship contribution statement

Mario Martínez: Methodology, Validation, Formal analysis, Investigation, Writing – original draft, Writing –review and rewriting. **Raúl López:** Resources, Supervision, Project administration. **J. Rodríguez:** Methodology, Writing –review and rewriting, Project administration, Funding acquisition. **Alicia Salazar:** Conceptualization, Methodology, Validation, Formal analysis, Writing – original draft, Writing –review and rewriting, Visualization, Supervision, Project administration.

Declaration of Competing Interest

The authors declare that they have no known competing financial interests or personal relationships that could have appeared to influence the work reported in this paper.

Acknowledgment

References

[1] P.M. Sforza, Chapter 12 - Solid Propellant Rocket Motors, in: P.M. Sforza (Ed.), Theory of Aerospace Propulsion, second ed., Butterworth-Heinemann, 2017, pp. 617–668.

[2] F. Xu, N. Aravas, P. Sofronis, Constitutive modeling of solid propellant materials with evolving microstructural damage, J. Mech. Phys. Solids. 56 (2008) 2050–2073.

[3] W.G. Knauss, On the Steady Propagation of a Crack in a Viscoelastic Sheet: Experiments and Analysis, in: H.H. Kausch, J.A. Hassell, R.I. Jaffee (Eds.), Deformation and Fracture of High Polymers, Springer, US, Boston, MA, 1973, pp. 501–541.

[4] R.A. Schapery, Correspondence principles and a generalized J integral for large deformation and fracture analysis of viscoelastic media, Int. J. Fract. 25 (1984) 195–223.

[5] C.D. Bencher, R.H. Dauskardt, R.O. Ritchie, Microstructural damage and fracture processes in a composite solid rocket propellant, J. Spacecr. Rockets. 32 (1995) 328–334.

[6] G.S. Tussiwand, V.E. Saouma, R. Terzenbach, L.T. De Luca, Fracture Mechanics of Composite Solid Rocket Propellant Grains: Material Testing, J. Propuls. Power. 25 (1) (2009) 60–73.

[7] S.D. Kim, D.H. Yoon, S.Y. Lee, J.H. Kim, Crack resistance behavior of particulate reinforced composites at various test speeds and temperatures, Materialwiss. Werkstofftech. 51 (2020) 603–612.

[8] M.N. Abdelaziz, R. Neviere, G. Pluvinage, Experimental investigation of fracture surface energy of a solid propellant under different loading rates, Eng. Fract. Mech. 31 (1988) 1009–1026.

[9] G. Zhou, X. Yin, A. Li, Study on the Fracture Toughness of Hydroxyl-Terminated Polybutadiene Solid Rocket Propellant, J. Propuls. Power. 31 (2015) 912–918.

[10] R. López, A. Ortega de la Rosa, A. Salazar, J. Rodríguez, Structural Integrity of Aged Hydroxyl-Terminated Polybutadiene Solid Rocket Propellant, J. Propuls Power. 34 (2018) 75–84.

[11] ASTM E1820-20b, Standard Test Method for Measurement of Fracture Toughness, 2020.

[12] H.A. Ernst, P.C. Paris, M. Rossow, J.W. Hutchinson, Analysis of Load-Displacement Relationship to Determine J-R Curve and Tearing Instability Material Properties, in: C.W. Smith (Ed.), ASTM International, West Conshohocken, PA, 1979, pp. 581–599.

[13] H.A. Ernst, P.C. Paris, J.D. Landes, Estimations on J-Integral and Tearing Modulus *T* from a Single Specimen Test Record, in: R. Roberts (Ed.), ASTM International, West Conshohocken, PA, 1981, pp. 476–502.

[14] M.H. Sharobeam, J.D. Landes, The load separation criterion and methodology in ductile fracture mechanics, Int. J. Fract. 47 (1991) 81–104.

[15] M.H. Sharobeam, J.D. Landes, The load separation and η_{pl}, Int. J. Fract. 59 (1993) 213–226.

[16] R. López, A. Salazar, J. Rodríguez, Fatigue crack propagation behaviour of carboxyl-terminated polybutadiene solid rocket propellants, Int. J. Fract. 223 (2020) 3–15.

[17] J. Xu, Y. Ju, B. Han, C. Zhou, J. Zheng, Research on relaxation modulus of viscoelastic materials under unsteady temperature states based on TTSP, Mech. Time Depend. Mater. 17 (2013) 543–556.

[18] STANAG 4506, Explosive Materials, Physical/Mechanical Properties Uniaxial Tensile Test, 2000.

[19] T.L. Anderson, Fracture Mechanics: Fundamentals and Applications, 4th ed., CRC Press, Boca Raton, FL, 2017.

[20] D.R. Moore, J.G. Williams, A. Pavan, Fracture Mechanics Testing Methods for Polymers, Adhesives and Composites, Elsevier Science & Technology, Oxford, 2001.

[21] Z. Wang, H. Qiang, G. Wang, Q. Huang, Tensile mechanical properties and constitutive model for HTPB propellant at low temperature and high strain rate, J. Appl. Polym. Sci. 132 (24) (2015).

[22] S.W. Park, Y. Richard Kim, R.A. Schapery, A viscoelastic continuum damage model and its application to uniaxial behavior of asphalt concrete, Mech. Mater. 24 (1996) 241–255.

[23] A. Salazar, J. Rodríguez, The use of the load separation parameter Spb method to determine the J-R curves of polypropylenes, Polym. Test. 27 (2008) 977–984.

[24] J.D. Landes, Z. Zhou, Application of load separation and normalization methods for polycarbonate materials, Int. J. Fract. 63 (1993) 383–393.

[25] B. Han, Y. Ju, C. Zhou, Simulation of crack propagation in HTPB propellant using cohesive zone model, Eng. Fail. Anal. 26 (2012) 304–317.

[26] A.A. Wells, Unstable crack propagation in metals: cleavage and fast fracture 1 (1961).